Chemical Engineering Science: X 4 (2019) 100043

Contents lists available at ScienceDirect

Chemical Engineering Science: X

journal homepage: www.elsevier.com/locate/cesx

Representative resolution analysis for X-ray CT: A Solid oxide fuel cell case study

T.M.M. Heenan, C. Tan, R. Jervis, X. Lu, D.J.L. Brett, P.R. Shearing [1]

Electrochemical Innovation Lab, Department of Chemical Engineering, UCL, London WC1E 7JE, UK
The Faraday Institution, Quad One, Harwell Science and Innovation Campus, Didcot OX11 0RA, UK

ARTICLE INFO

Article history:
Received 10 April 2019
Received in revised form 19 June 2019
Accepted 5 October 2019

Keywords:
Solid oxide fuel cell
X-ray computed tomography
Triple-phase boundary
Fractal
Resolution

ABSTRACT

A requirement to reduce dependency on high-carbon fuels has resulted in the rapid advancement of electrochemical devices. Considerable research has been applied to improve device performance and lifetime in order to compete with incumbent technologies. Of the portfolio of electrochemical conversion technologies, solid oxide fuel cells (SOFC) offer high fuel versatility and fast reaction kinetics without the requirement of expensive catalysts. However, degradation due to high temperature operation limits cell performance and lifetime, impeding widespread commercialisation. Due to the inherent link between microstructure and electrochemical performance, many three-dimensional (3D) characterisation techniques have been employed in the pursuit of the mitigation of degradation through rational electrode design. Instruments such as lab-based X-ray microscopes are now capable of imaging across multiple length scales, where the highest resolutions (i.e. smallest voxel lengths) are comparable to specialist synchrotron facilities. A widely used metric to describe electrode microstructure is the triple-phase boundary (TPB); the location where reactions occur within the SOFC electrode. The total TPB length is a vital metric in assessing the quality of an SOFC material, and thus many efforts have been made to determine accurate values. In order to map the TPB locations in 3D, the three constituent phases: metal, ceramic, and pore, need to be distinguished and segmented, requiring high resolutions. Although TPB values have been reported and compared extensively in the literature, the influence of the microscopic roughness is yet to be investigated. Using X-ray computed tomography (CT), here, for the first time, the effect of resolution is inspected for several key microstructural parameters. Moreover, the study is extended through the use of multiple instruments for a variety of sample structures. This work introduces the importance of the fractal properties of structures characterised using X-ray CT, which we expect to be influential across a broad range of materials. The choice of resolution when characterising a structure is important and determined by a variety of factors: instrument, feature size, image quality, etc., and should ultimately be chosen in order to efficaciously expose the features under investigation, in addition to this, metrics extracted should only be directly compared at the same resolution and, if possible, should be inspected for fractal properties via a representative resolution analysis. These conclusions are not restricted to SOFCs but should be applied to all fields of microstructural analysis.

1. Introduction

Solid oxide fuel cells (SOFCs) are electrochemical energy conversion devices that offer fuel versatility and high electrical efficiencies, operating at high temperatures (600–1000 °C) without the need for precious metal catalysts. They require high power densities with minimal degradation over long lifetimes in order to compete with existing technologies. Degradation mechanisms have been investigated extensively in an effort to extend device lifetimes (Ormerod, 2003; Scrosati, 2000; Gottesfeld and Zawodzinski, 1997), and rational electrode design strategies have

Abbreviations: SOFC, Solid Oxide Fuel Cell; 3D, Three-Dimensional; TPB, Triple-Phase Boundary; CT, Computed Tomography; FIB-SEM, Focused Ion Beam Scanning Electron Microscope; Ni, Nickel; YSZ, Yttria-Stabilised Zirconia; ROI, Region of Interest; RVE, Representative Volume Element; RRE, Representative Resolution Element; LFOV, Large Field of View; HRes, High Resolution; FDK, Feldkamp-Davis-Kress.

[1] Address: The Electrochemical Innovation Lab, Department of Chemical Engineering, University College London, WC1E 7JE, UK.
E-mail address: p.shearing@ucl.ac.uk (P.R. Shearing)

https://doi.org/10.1016/j.cesx.2019.100043
2590-1400/

been pursued for the improvement of device power densities (Guo et al., 2008; Zhu and Deevi, 2003; Serov and Kwak, 2009).

High temperature operation can induce metal sintering during long-term operation as well as mechanical degradation, particularly prevalent during start-up and shut-down: both of which have been shown to reduce electrochemical performance and lifetime (Zekri et al., 2017; Park et al., 2010). Electrochemical performance is strongly dependent upon microstructure, particularly the distribution of reaction sites connected to percolated transport networks. The reaction site is located where the three transport networks meet: the electron conducting metal, the ion conducting ceramic, and gases within the pore, and is named the triple-phase boundary (TPB) which is characterised by a one dimensional length, L_{TPB}, typically reported as a value corrected with respect to the electrode volume analysed, ρ_{TPB}. This value can be further characterised into sites which are either active or inactive according to the percolation of the three constituent phases to/from the reaction site; if all three phases are percolated the site is considered active, if one or more of the phases are not percolated the site is considered inactive. The active reaction sites are named percolated TPBs and are denoted, ρ^{P}_{TPB}, and are often compared to the total reaction sites, ρ^{T}_{TPB}, through a percolation percentage, P_{TPB} (Golbert et al., 2008).

The volumetric density of the active reaction sites, and thus the performance of the cell, is expected to reduce over the lifetime of the cell due to mechanisms such as the aforementioned sintering and mechanical degradation (Zekri et al., 2017; Park et al., 2010; Heenan et al., 2018). Due to this inherent link between microstructure and electrochemical performance, 3D characterisation has become a prominent focus of SOFC research. Nickel (Ni) and yttria-stabilised zirconia (YSZ) are commonly employed as the metal and ceramic, respectively, within the SOFC anode in the form of a porous Ni-YSZ cermet, and was first mapped in 3D by Wilson et al. (2006) through the use of a focused ion beam scanning electron microscope (FIB-SEM). Although successful in mapping the TPB reaction sites in 3D, FIB-SEM is a destructive technique that prevents repeated studies on the same region of interest (ROI). In order to track microstructural degradation within the same ROI, non-destructive techniques such as X-ray computed tomography (CT) therefore became favourable. However, in order to obtain sufficient resolution and contrast, this technique has historically required the use of high-brilliance X-ray sources at specialist synchrotron facilities (Shearing et al., 2009; Guan et al., 2011; Laurencin et al., 2012). Although lab-based X-ray CT had previously been demonstrated for two phases, solid and pore, (Izzo et al., 2008; Shearing et al., 2010), it is only recently that we have been able to produce three-phase segmentation using lab-based nano-CT (Heenan et al., 2017). Since then, the ready availability of lab-based three-phase segmentations has resulted in improved microstructural characterisation and electrochemical modelling through the incorporation of real microstructures (Heenan et al., 2018; Lu et al., 2018).

There are several examples from the literature of how electrochemical modelling has been enhanced through the use of X-ray CT; for instance the extraction of tortuosity information, often in the form of a tortuosity-factor, τ, (Tjaden et al., 2018) has improved the accuracy of the prediction of effective transport properties such as diffusivity and electrical and ionic conductivities. Furthermore, the incorporation of characterisation across multiple length-scales has allowed diffusion modelling to accommodate continuum physics through to Knudsen flow *via* real microstructures (Lu et al., 2018).

Whilst TPB density has become a common metric for the evaluation and comparison for SOFC electrodes, studies into the effect of imaging resolution (voxel length) on the extracted metrics from tomographic data remain limited (Shah et al., 2016). As TPB density has emerged as a key metric of cell performance models (Golbert et al., 2008; Timurkutluk and Mat, 2016), it is imperative to ensure accuracy in the comparison of different ρ_{TPB} values.

It has previously been observed that the ρ_{TPB} value quantified for the same sample at higher resolutions (smaller voxel lengths) consistently results in a higher reaction site density (Heenan et al., 2017). Building upon this, Bertei *et al.* investigated the influence of resolution on the reaction site density by the definition of a TPB fractal dimension obtained through FIB-SEM characterisation (Bertei et al., 2017), which was then employed to improve an electrochemical model. This fractal relationship between resolution and characterised length is based upon work by Mandelbrot, whereby a measured length increases in detail, and thus magnitude, with increasing resolution (Mandelbrot, 1967; Mandelbrot et al., 1984). Subsequently, fractal properties have been extensively reported from biological samples to industrial catalysts (Zhou et al., 2018; Tikhomirov et al., 2017; Kirchner et al., 2000; Miller et al., 2017); however, knowledge of the fractal properties of electrochemical materials remains very limited.

The validity of microstructural data incorporated into electrochemical models must be ensured in order to provide confidence in their predictions. With the increasing adoption of multi-length scale X-ray CT characterisation, it is important to establish rigour in the comparisons of structural metrics such as the TPB, and gain insight into the influence of the characterisation resolution, i.e. voxel length, employed. In order to improve the statistical relevancy of data, representative volume element (RVE) analysis computations have become standard practice (Heenan et al., 2017). Looking forward, we may see representative resolution element (RRE) analysis computation, such as those presented here, becoming commonplace in the quantification of data obtained from tomography techniques; not only using X-ray absorption but also other forms of tomography such as neutron, X-ray diffraction and X-ray fluorescence.

In this work, the influence of image resolution is inspected for several key metrics in electrochemical modelling of SOFC electrodes and, for the first time, the fractal dimension is extracted from several SOFC electrodes of varying microstructures using lab-based X-ray CT. This work demonstrates the importance of the fractal properties of metrics characterised using X-ray CT, not limited to SOFC electrodes but across the field of X-ray CT characterisation of electrochemical materials.

2. Materials and methods

2.1. Materials and sample preparation

Porous Ni metal (Novamet Specialty Products Corp, Lebanon) and NiO-YSZ cermet (Fuel Cell Materials, OH, USA) powders were pressed into cylindrical pellets under isostatic compression. Once formed, the pellets were sintered for 2.5 h at 1200 °C in air and subsequently reduced to Ni and Ni-YSZ for 2 h at 800 °C in forming gas (4% H_2 in 96% N_2). All samples were prepared by extracting small particles from the material bulk using a sharp scalpel and attached to the top of a pin using fast-set epoxy (Heenan et al., 2017). Samples for nano- and micro-CT analysis were prepared with diameters of ca. 40 μm and 400 μm, respectively, using a sharp scalpel.

2.2. X-ray CT

Lab-based micro-CT was achieved through the use of an Xradia 520 VERSA X-ray instrument (Zeiss 520 VERSA, Carl Zeiss inc., CA, USA). This technique employs a cone-beam geometry with coupled

Table 1
Case study summary with sample breakdown, instrument employed in acquisition and the resolution at which the analysis was performed represented by an isotropic voxel length.

Case Study #	Sample #	Material(s)	Dataset #	Instrument	Analysis Resolution/nm
1	1	Porous Ni	1	VERSA 20X	800
			2	VERSA 40X	400
2	2	Porous Ni-YSZ	3	ULTRA HRes	32
			4	ULTRA Hres Binned	64
			5	ULTRA LFOV	130
			6	ULTRA LFOV Binned	260
3	3	Porous Ni-YSZ	7	ULTRA HRes	32
		Porous Ni-YSZ	8	ULTRA Hres Binned	50
		Porous Ni-YSZ	9	ULTRA Hres Binned	75
		Porous Ni-YSZ	10	ULTRA Hres Binned	100
		Porous Ni-YSZ	11	ULTRA Hres Binned	125
		Porous Ni-YSZ	12	ULTRA LFOV	126
		Porous Ni-YSZ	13	ULTRA LFOV Binned	175
		Porous Ni-YSZ	14	ULTRA LFOV Binned	200
		Porous Ni-YSZ	15	ULTRA LFOV Binned	250
	4	Porous Ni-YSZ	16	ULTRA HRes	32
		Porous Ni-YSZ	17	ULTRA Hres Binned	50
		Porous Ni-YSZ	18	ULTRA Hres Binned	75
		Porous Ni-YSZ	19	ULTRA Hres Binned	100
		Porous Ni-YSZ	20	ULTRA Hres Binned	125
		Porous Ni-YSZ	21	ULTRA LFOV	126
		Porous Ni-YSZ	22	ULTRA LFOV Binned	130
		Porous Ni-YSZ	23	ULTRA LFOV Binned	150
4	5	Porous Ni-YSZ	24	ULTRA LFOV Binned	250
		Porous Ni-YSZ	25	ULTRA LFOV Binned	275
		Porous Ni-YSZ	26	ULTRA LFOV Binned	300
		Porous Ni-YSZ	27	ULTRA LFOV Binned	325
		Porous Ni-YSZ	28	ULTRA LFOV Binned	350
		Porous Ni-YSZ	29	ULTRA LFOV Binned	375
		Porous Ni-YSZ	30	ULTRA LFOV Binned	400
		Porous Ni-YSZ	31	ULTRA LFOV Binned	425
		Porous Ni-YSZ	32	ULTRA LFOV Binned	450
		Porous Ni-YSZ	33	ULTRA LFOV Binned	475
		Porous Ni-YSZ	34	ULTRA LFOV Binned	500

geometric and optical magnification, yielding two magnifications used here, namely, 40X and 20X, both with a binning of 2 applied during acquisition with voxel lengths of 400 nm and 800 nm, respectively. Nano-CT was conducted using a lab-based Xradia 810 ULTRA X-ray instrument (Zeiss 810 Ultra, Carl Zeiss inc., CA, USA) employing a parallel-beam geometry coupled to a Fresnel zone plate focussing architecture with two magnifications; namely, large field of view (LFOV) and high resolution (HRes), both with a binning of 2 applied during acquisition achieving voxel lengths of 126 nm and 32 nm, respectively. Reconstruction was accomplished using Feldkamp-Davis-Kress (FDK) and filtered back-projection algorithms for the cone- and parallel-beam datasets, respectively, using commercial software ('Reconstructor Scout-and-Scan', Carl Zeiss Inc., CA, U.S.A.). All imaging information can be found in Table 1.

2.3. Resolution resampling and segmentation

In order to obtain data with reduced resolution, each greyscale tomogram was 'binned' after reconstruction by combining two or more voxels into one voxel of larger dimension via the averaging of the data within the combined voxels. This was achieved using 'resampling' algorithms based upon this method in Avizo Fire software (Avizo, Thermo Fisher Scientific, Waltham, Massachusetts, U.S.). Avizo Fire software was also employed for the segmentation of the data sets into the constituent material phases: metal and pore for porous Ni pellets and metal, ceramic and pore for the porous cermet pellets *via* thresholding of the 3D greyscale histogram. Visual examples of data binning procedures can be found in the supplementary information.

2.4. Quantification of microstructural properties

After segmentation, the composition, tortuosity and percolation were quantified in the form of volume fractions, V_{phase}, directional tortuosity-factors, τ_{phase_C}, and percolation values, p_{phase_C}, with respect to the Cartesian directional orientation, C = x, y or z. These were obtained using TauFactor (Cooper et al., 2016), an open source Matlab application.

Experimental observations by *Yousuf et al.* produced a relationship for Ni resistivity with temperature (Yousuf et al., 1986), the inverse of which can be used to obtain the Ni electrical conductivity, σ_{ele}. Using the directional tortuosity-factor, τ_{NiC}, and volume fraction, V_{Ni}, an effective electrical conductivity can be obtained, $\sigma^{Eff}_{ele,C}$, encompassed in Eq. (1):

$$\sigma^{Eff}_{ele,C} = \frac{V_{Ni}}{\tau_{NiC}} \cdot \left(\frac{T^2}{9.362 \times 10^6} + \frac{T}{6.972 \times 10^3} + 20.654 \cdot \left[1 + \frac{T - 630}{8.1 \times 10^4} \right] \right)^{-1} \quad (1)$$

Eq. (1) approximates the electrical conductivity at operating temperature. The Ni metal is supplied above 99.5% purity and is exposed to minimal thermal history prior to characterisation, therefore Eq. (1) is assumed to suitably represent the metal conductivity.

The ionic conductivity of oxide ions within YSZ, σ_{ion}, was predicted using an exponential function (Zhu and Kee, 2003; Iwai et al., 2010; Shearing et al., 2010), with adjustment to obtain an effective ionic conductivity, $\sigma^{Eff}_{ion,C}$, using the directional tortuosity-factor, τ_{YSZC}, and volume fraction, V_{YSZ} of the ceramic, resulting in Eq. (2):

$$\sigma_{ion,C}^{Eff} = \frac{V_{YSZ}}{\tau_{YSZ\,C}} \cdot \frac{\sigma_{ion}^{0}}{T} \cdot \exp\left(-\frac{E_{io}}{RT}\right) \quad (2)$$

Values of 3.6×10^{7} S m^{-1} and 8.0×10^{4} J mol^{-1} were employed for the pre-exponential factor, σ_{ion}^{0}, and ionic transport activation energy, E_{io}, respectively for all ionic calculations (Iwai et al., 2010).

The triple-phase boundary density, ρ_{TPB}, was calculated using two techniques; the aforementioned TauFactor application and an established Matlab algorithm (Cooper et al., 2016; Lu et al., 2017). TauFactor was employed to compare two samples of different microstructures and the Matlab algorithm was employed to inspect the same sample obtaining both percolated, ρ_{TPB}^{P}, and total, ρ_{TPB}^{T}, TPB density values. When comparing two samples with different Ni microstructures, the particle Feret diameters, d_f, were calculated using ImageJ software (Rueden et al., 2017), whereby the Feret diameter is defined as the largest cross-sectional length of a particle (Shearing et al., 2010).

2.5. Resolution analysis and fractal properties

Effective conductivities were computed using the volume fractions and tortuosity-factors for each voxel length for both micro- and nano-CT tomograms to review the effects of the characterisation voxel length on the resulting effective conductivity. The reaction site density was also calculated for each voxel length to inspect the effects of resolution. The ρ_{TPB} values were then plotted on log-log axes in order to obtain a fractal dimension, D, and linear scaling factor, f, using the Mandelbrot relation as explained by Bertei et al. (2017), presented in Eqs. (5) and (6) whereby the resolution, r, is presented as the isotropic voxel length.

$$\rho_{TPB} = f \cdot r^{1-D} \quad (5)$$

$$Log_{10}(\rho_{TPB}) = f + (1 - D) \cdot Log_{10}(r) \quad (6)$$

3. Results and discussion

3.1. Predicting the effective electrical conductivity of Ni using cone-beam X-ray micro-CT at two resolutions

For materials of similar attenuation coefficient (Heenan et al., 2017) two-phase segmentation is considerably easier than three-phase segmentation; three-phase segmentation using micro-CT often requires the use of greyscale fiducial markers (Heenan et al., 2018); whereas nano-CT using a monochromatic or even quasi-monochromatic beam can be archived directly from the materials of interest, i.e. without the use of a fiducial (Heenan et al., 2017). In this first case study, the effective electrical conductivity of porous Ni is examined at two resolutions using X-ray micro-CT using a lower resolution (800 nm voxel length) tomography followed by a ROI scan of the same sample at a higher resolution (400 nm voxel length).

All characterised metrics can be found in Table 2. The Ni phase tortuosity is significantly higher for the lower resolution tomogram, i.e. $\tau_{Ni\ 800\ nm} > \tau_{Ni\ 400\ nm}$, regardless of directional orientation and the directional trend remains: i.e. $\tau_{Ni,x} > \tau_{Ni,y} > \tau_{Ni,z}$ for both 400 nm and 800 nm voxel lengths. Although the general structure remains similar in both the 400 and 800 nm resolution tomograms, the higher resolution 400 nm tomogram exposes particles that went previously undetected within the 800 nm resolution tomogram due to partial averaging. These small particles may complete previously more tortuous paths in a shorter distance, hence reducing the overall tortuosity factor.

Unlike tortuosity, the effect of resolution on the two-phase composition is negligible, observing a variation by only ca. 2%. These values were then inserted into Eq. (1) in order to inspect variation of the electrical conductivity with temperature for the three orientations. Deviations in the tortuosity-factor and composition with resolution are displayed in Fig. 1, accompanied by the effective conductivity (plotted as a function of temperature for the different resolution scans); the latter is also tabulated fully in Table 3. These factors result in a difference between the effective conductivity characterised with voxel lengths of 400 nm and 800 nm of 28%, 20% and 14% in the x, y and z orientations, respectively. These are considerable discrepancies; however, resistance attributed to the electrical transport in Ni is typically assumed to be negligible compared to the resistance to ion transport within the ceramic. Therefore, although the voxel length employed in characterising the Ni properties can strongly influence the effective conductivity, electrical conductivity values remain orders of magnitude larger than that which are attributed to ionic transport.

3.2. Predicting the effective ionic conductivity of 8YSZ using parallel-beam X-ray nano-CT at four resolutions

This second case study employs a quasi-monochromatic beam, allowing the segmentation of the three constituent phases: Ni, YSZ and pore without the need for a fiducial material (Heenan et al., 2017). As a result, the effective oxide ion conductivity within porous Ni-YSZ is inspected at four resolutions using parallel-beam X-ray nano-CT. Ion conduction is assumed to only occur within the ceramic phase, therefore only YSZ is characterised.

Firstly, the ceramic tortuosity-factor reduces with increasing voxel lengths $\tau_{YSZ\ 260\ nm} < \tau_{YSZ\ 130\ nm} < \tau_{YSZ\ 64\ nm} < \tau_{YSZ\ 32\ nm}$. Since this material contains three phases, the percolation values are also inspected; the YSZ percolation is independent of directional orientation i.e. $p_{YSZ\,x} = p_{YSZ\,y} = p_{YSZ\,z}$ for resolutions from 32 nm to 260 nm to 1 d.p. The tortuosity-factor and percolation values are presented in Table 4. Although these values are directionally heterogeneous, the effects of resolution on the degree of heterogeneity are minor. Furthermore, through a voxel length change from 32 nm to 260 nm, an increase of 20%, 12% and 22% in conductivity is observed in the x, y and z directions respectively. Hence, resolution considerably affects the prediction of oxide anion conductivity within YSZ; the effective conductivity is presented for various temperatures and resolutions in Fig. 2.

Table 2
Microstructural properties for porous Ni obtained via micro-CT with two isotropic voxel lengths: 400 and 800 nm.

	Voxel Length/nm	Tortuosity, τ_{Ni} / no-units				Volume Fraction / $\mu m^3 \cdot \mu m^{-3}$
		x	y	z	Avg.	
Ni	400	2.43	2.15	2.07	2.22	0.53
	800	3.38	2.70	2.41	2.83	0.51
Pore	400	3.04	2.81	2.11	2.65	0.47
	800	2.86	2.67	2.04	2.52	0.49

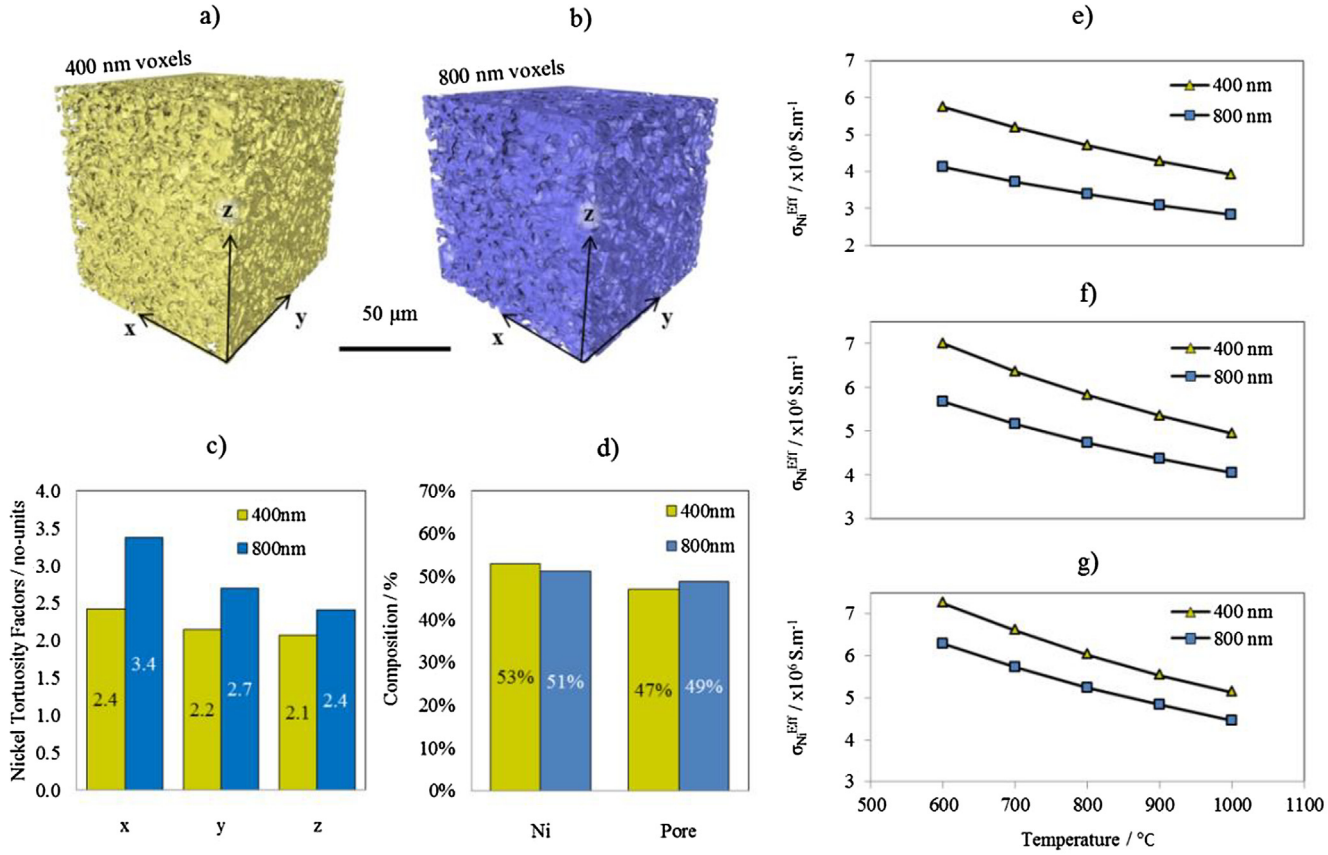

Fig. 1. Influence of resolution on the effective electrical conductivity of Ni metal: 3D surface generations from tomograms obtained using cone-beam X-ray micro-CT with two voxel lengths (a) 400 nm and (b) 800 nm, with accompanying (c) directional tortuosity-factors, (d) phase compositions and directional effective conductivities in the (e) x, (f) y, and (g) z directions.

Table 3
Effective electrical conductivity values for Ni calculated for the operating temperatures of SOFCs corrected using microstructural data obtained via micro-CT with two data sets of isotropic 400 nm and 800 nm voxel lengths.

Temperature / °C	σ_x/×10^6 S m^{-1}		σ_y/×10^6 S m^{-1}		σ_z/×10^6 S m^{-1}	
	400 nm	800 nm	400 nm	800 nm	400 nm	800 nm
600	5.75	4.13	6.50	5.17	6.75	5.80
700	5.19	3.73	5.86	4.67	6.09	5.23
800	4.71	3.38	5.32	4.24	5.53	4.75
900	4.29	3.09	4.85	3.86	5.04	4.33
1000	3.93	2.83	4.45	3.54	4.62	3.97
Offset	28%		20%		14%	

Table 4
Microstructural properties for YSZ within a porous Ni-YSZ cermet anode obtained via nano-CT using four voxel lengths, 32, 64, 130 and 260 nm.

Voxel Length / nm	Tortuosity, τ_{YSZ} / no-units				Percolation, p / %				Volume Fraction / µm^3·m^{-3}
	x	y	z	Avg.	x	y	z	Avg.	
32	1.93	1.66	2.11	1.90	99.4	99.4	99.4	99.4	0.18
64	1.74	1.44	1.74	1.64	99.7	99.7	99.7	99.7	0.17
130	1.65	1.50	1.77	1.64	99.7	99.7	99.7	99.7	0.20
260	1.54	1.46	1.65	1.55	99.9	99.9	99.9	99.9	0.19

The reducing tortuosity factor with increasing voxel length may be due to the same reason that the metallic tortuosity factor increases within Case Study 1 but in reverse; partial averaging at lower resolutions closes spaces between the YSZ particles that are actually pores/voids, which is only exposed at higher resolutions. This increases the path length of the YSZ or possibly even isolates particles entirely. This is corroborated by the increased percolation at lower resolutions.

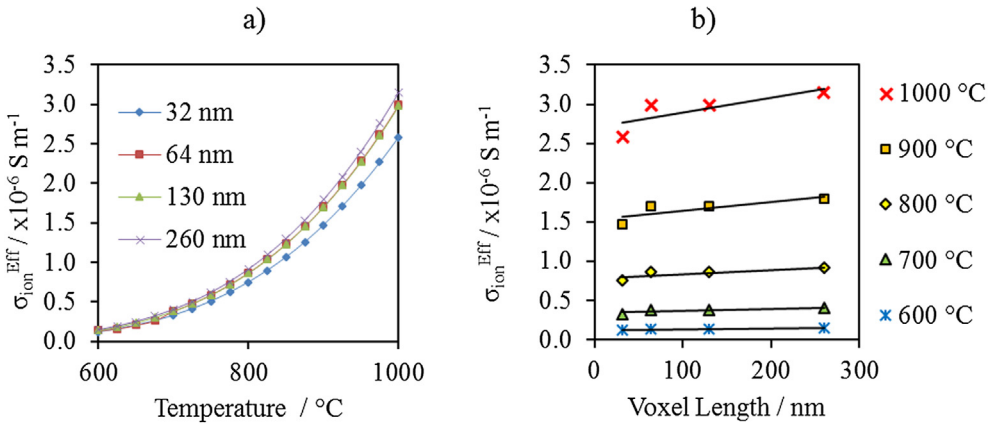

Fig. 2. Effective ionic conductivity values for YSZ calculated for the operating temperatures of SOFCs corrected using microstructural data obtained via nano-CT using four voxel lengths, 32, 64, 130 and 260 nm: (a) variation in the effective ionic conductivity within YSZ with temperature for various resolutions, and (b) variation in the effective ionic conductivity within YSZ with resolution for various temperatures.

Table 5
Average particle Feret diameters for Ni, YSZ and pore within a cermet anode obtained via nano-CT using HRes imaging at an isotropic voxel length of 32 nm.

	Feret Diameter, d_f / μm			ρ_{TPB} / μm^{-2}
	Ni	YSZ	Pore	
Sample 1	1.1	1.0	2.6	6.87
Sample 2	1.8	1.0	2.7	3.17

3.3. Extracting the reaction site fractal dimension and roughness factor for two samples of varying Ni microstructure

Two lab-based X-ray nano-CT characterisation methods are compared: LFOV and HRes. The comparison is extended through the analysis of two porous Ni-YSZ samples with varying Ni microstructure, representative of the result of possible fuel cell degradation mechanisms. The variation in the two samples is quantified by the average particle Feret diameter for each phase and the TPB density, which are all characterised using tomograms with 32 nm isotropic voxel lengths and presented in Table 5.

Through application of the Mandelbrot relationship (Eqs. (5) and (6)), the fractal dimensions of the two samples were extracted with accompanying linear scaling factors, values were obtained from the two samples for both LFOV and HRes and are all presented in Table 6. Minor variation was observed between the $D_{1,LFOV}$ and $D_{1,HRes}$ fractal dimensions for sample 1: 2.31 and 2.14, similarly the fractal dimension for the second sample was similar for both $D_{2,LFOV}$ and $D_{2,HRes}$: 1.79 and 1.88. The linear scaling factors showed an equivalent trend; f_{LFOV} and f_{HRes} values were similar but varied between samples. These values are similar to those which have previously been reported by Bertei *et al.* (Bertei et al., 2017).

These techniques consistently produce fractal properties, even for very different microstructures. The fractal properties are therefore dependent upon the microstructure inspected i.e. each sample inspected will likely have a unique fractal dimension and linear scaling factor; however, the properties extracted from a sample are relatively independent of the characterisation technique employed i.e. the same sample imaged at LFOV and HighRes produced comparable fractal properties. This is visualised in Fig. 3 whereby the gradients of the two linear plots on the log-log axes for HRes and LFOV are very similar for the same sample, but differ between samples.

Table 6
Fractal properties for the reaction site densities within porous Ni-YSZ cermet anodes of varying Ni microstructure obtained via nano-CT using two imaging methods: HRes and LFOV.

	Sample 1		Sample 2	
	HRes	LFOV	HRes	LFOV
Gradient, m	−1.14	−1.31	−0.88	−0.79
fractal dimension, D	2.14	2.31	1.88	1.79
Linear scaling factor, f	2.54	2.99	1.81	1.61
Coefficient of determination, R^2	0.99	0.97	0.99	1.00

All four sets of fractal properties presented coefficients of determination above 0.97, indicating that the fractal properties were highly log-linear, and safely within the 'fractal domain'. It should also be noted that, as with other fractal systems, there will be a maximum voxel-size whereby the dependency of the resolution on the fractal property will diverge from a logarithmic relationship and no longer represent the data, i.e. leave the fractal domain. However, a significant number of the voxels are often used to compose a single feature using tomography and, although sample dependant, the voxel-size limits are likely to be significantly larger than that employed, so long as features can be resolved. Similarly, the RVE criteria should still be met, regardless of the resolution employed. See work by Bouchaud et al. for an example on the study of the stability of the fractal dimension and the range of the fractal domain (Bouchaud et al., 1990).

3.4. Extracting the total and percolated reaction site fractal dimension and roughness factors

The effects of resolution on the degree of reaction site isolation were inspected for a porous Ni-YSZ electrode using the X-ray nano-CT technique in the LFOV imaging mode. It was found that the percentage of reaction sites which are percolated remains relatively unchanged regardless of resolution: P_{TPB} = 90%. Whilst the fractal dimension and the linear scaling factor differ between percolated and total reaction sites, both relationships display high linearity as with the previous two samples, with coefficient of determination values of 1.00–2 d.p. The fractal information is presented in Table 7 along with the TPB density variation with resolution in Fig. 4.

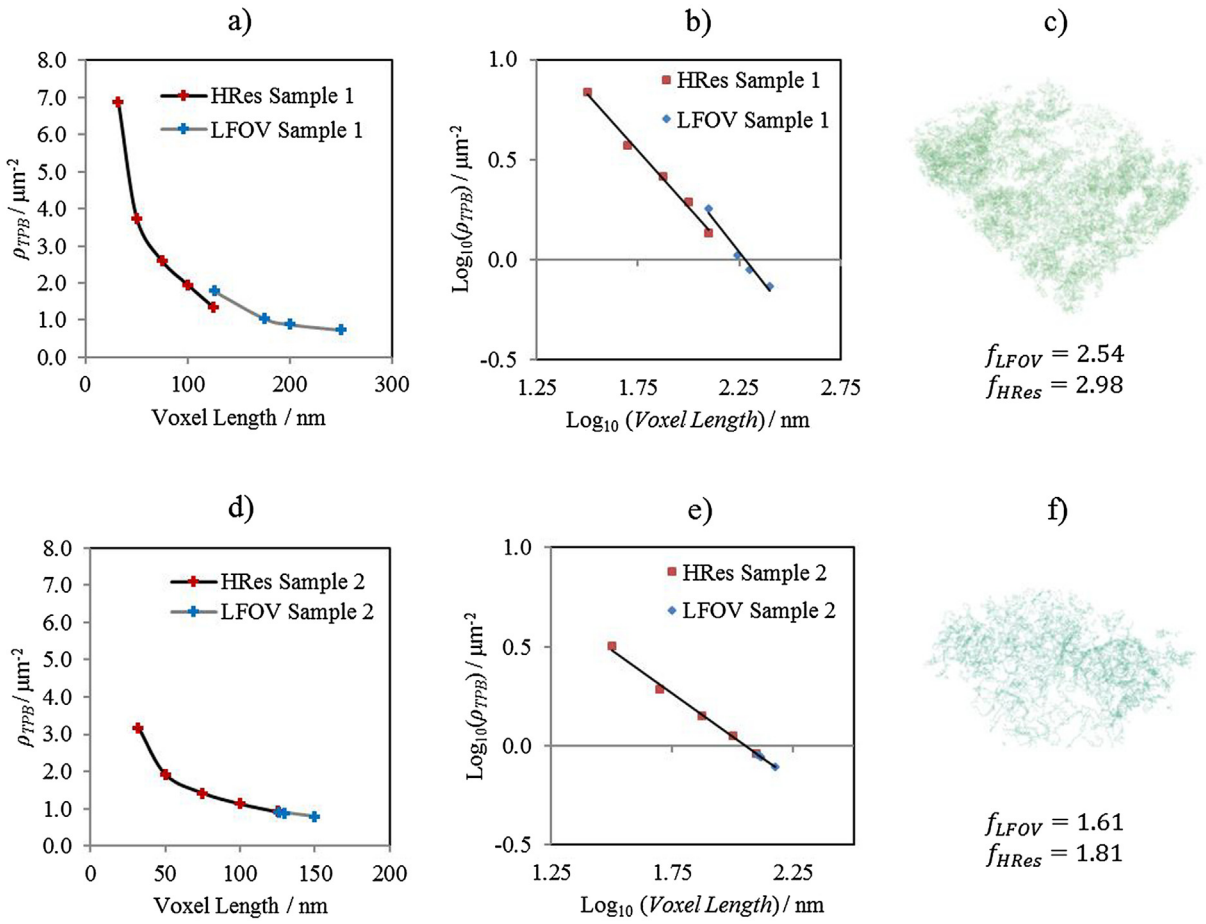

Fig. 3. Inspecting the influence of voxel length when characterising the TPB within SOFC anodes by comparing two samples of differing Ni microstructure: (a) TPB density variation with voxel length for sample 1, (b) plotted on a log-log axes, with (c) accompanying 32 nm voxel length TPB map and roughness factors for the two imaging methods, (d) TPB density variation with voxel length for sample 2, (e) plotted on a log-log axes, with (f) accompanying 32 nm voxel length TPB map and roughness factors for the two imaging methods.

Table 7
Fractal properties for the total and percolated reaction site densities within a porous Ni-YSZ cermet anode obtained via LFOV nano-CT.

	Total	Percolated
Gradient,*m*	−1.20	−1.21
fractal dimension,*D*	2.20	2.21
Linear scaling Factor,*f*	2.49	2.47
Coefficient of determination, R^2	1.00	1.00

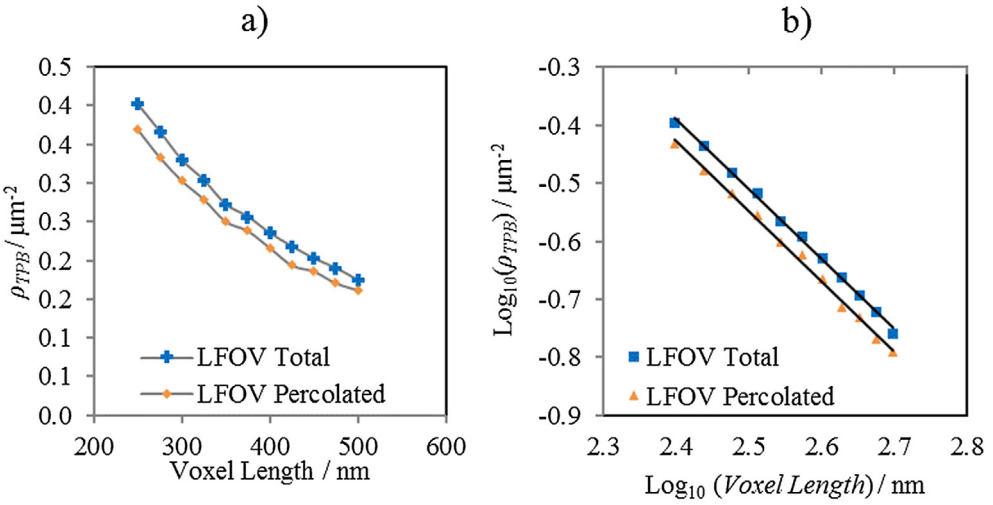

Fig. 4. Inspecting the influence of voxel length when characterising the TPB within an SOFC anode by comparing the total and percolated reaction site densities: (a) total and percolated TPB density variation with voxel length obtained using LFOV, and (b) total and percolated TPB density variation with voxel length plotted on a log-log axes for the application of the Mandelbrot relationship.

4. Conclusion

Three-dimensional characterisation can provide powerful insight into performance and degradation in electrochemical devices. X-ray CT has become widely used as a characterisation technique in the non-destructive extraction of microstructural data, but the portfolio of instruments available provide a spectrum of resolution capabilities. In order to inspect the effects of such variation in resolution (or voxel length) on the properties obtained from electrochemical devices, several important properties have been extracted from a variety of SOFC anode materials as a case study.

Predictions of the effective electrical conductivity are found to be significantly influenced by resolution, though resistances attributed to electron transport remain negligible compared to the transport of oxide ions. Moreover, the influence of resolution on the effective ionic conductivity is also considerable although the influence of temperature remains most prominent. The Mandelbrot relation has been used to inspect the fractal properties of the reaction sites within SOFC anodes characterised using X-ray CT. Fractal dimensions greater than unity are observed for all samples using all techniques; reaction site densities characterised at different resolutions cannot be directly compared without the incorporation of fractal properties. The Ni particle size can influence the fractal properties of the TPB reaction site resulting in different fractal dimensions and linear scaling factors for different microstructures. Although varying between samples, the fractal properties extracted from different techniques produce comparable results; i.e. high magnification may be used to extrapolate apparent reaction site densities at lower resolutions, likewise the low magnification may be used to extrapolate apparent reaction site densities at higher resolutions. The degree of reaction site percolation may not be influenced by resolution but results in distinct fractal dimensions for the total and percolated TPB densities; the fractal properties of the percolated and isolated reaction sites may differ.

The influence of resolution on extracted metrics is not limited to SOFC but may apply across the field of X-ray microscopy. Ultimately the choice of resolution when characterising a structure is highly important, generally, one should aim to collect data with a spatial resolution significantly higher than the feature of interest, i.e. a voxel length much smaller than the particle diameter. Although, trade-offs between sufficient statistical representation and, spatial and temporal resolutions, along with efforts to optimise signal to noise, often influence resolution choice during characterisation. Furthermore, when comparing a variable from two or more datasets of differing resolutions the variable of interest should be inspected for fractal properties before a direct comparison can be carried out. Analogous to the statistical representation that is confirmed using an RVE analysis, the representative resolution should be assessed via RRE analysis techniques such as those that are discussed here. The extraction of fractal properties may not only improve the validity of instrument-to-instrument comparisons but also the accuracy of electrochemical simulations aiding in high-precision predictive modelling.

CRediT authorship contribution statement

T.M.M. Heenan: Conceptualization, Data curation, Formal analysis, Investigation, Methodology, Validation, Visualization, Writing - original draft, Writing - review & editing. **C. Tan, R. Jervis, X. Lu:** Validation, Writing - original draft, Writing - review & editing. **D.J. L. Brett, P.R. Shearing:** Conceptualization, Funding acquisition, Project administration, Resources, Software, Supervision, Validation, Writing - original draft, Writing - review & editing.

Declaration of Competing Interest

The authors declare that they have no known competing financial interests or personal relationships that could have appeared to influence the work reported in this paper.

Acknowledgements

The authors would like to acknowledge the EPSRC (EP/M014045/1), the Centre for Doctoral Training (EP/L015749/1), financial support from the Royal Academy of Engineering (CiET1718\59) and the Faraday Institution (faraday.ac.uk; EP/S003053/1), grant number FIRG001; access to the Xradia 520 VERSA instrument was supported by EPSRC (EP/N032888/1) and access to the Xradia 810 Ultra 810 instrument was supported by the EPSRC (EP/K005030/1).

Appendix A. Supplementary material

Supplementary data to this article can be found online at https://doi.org/10.1016/j.cesx.2019.100043.

References

Bertei, A., Ruiz-Trejo, E., Kareh, K., Yufit, V., Wang, X., Tariq, F., Brandon, N.P., 2017. The Fractal nature of the three-phase boundary: a heuristic approach to the degradation of nanostructured solid oxide fuel cell anodes. Nano Energy 38, 526–536.

Bouchaud, E., Lapasset, G., Planes, J., 1990. Fractal dimension of fractured surfaces: a universal value?. EPL (Europhys. Lett.) 13 (1), 73.

Cooper, S.J., Bertei, A., Shearing, P.R., Kilner, J.A., Brandon, N.P., 2016. TauFactor: an open-source application for calculating tortuosity factors from tomographic data. SoftwareX 5, 203–210.

Golbert, J., Adjiman, C.S., Brandon, N.P., 2008. Microstructural modeling of solid oxide fuel cell anodes. Ind. Eng. Chem. Res. 47 (20), 7693–7699.

Gottesfeld, S., Zawodzinski, T.A., 1997. Polymer electrolyte fuel cells. Adv. Electrochem. Sci. Eng. 5, 195–302.

Guan, Y., Li, W., Gong, Y., Liu, G., Zhang, X., Chen, J., Gelb, J., Yun, W., Xiong, Y., Tian, Y., Wang, H., 2011. Analysis of the three-dimensional microstructure of a solid-oxide fuel cell anode using nano X-ray tomography. J. Power Sour. 196 (4), 1915–1919.

Guo, Y.G., Hu, J.S., Wan, L.J., 2008. Nanostructured materials for electrochemical energy conversion and storage devices. Adv. Mater. 20 (15), 2878–2887.

Heenan, T.M., Bailey, J.J., Lu, X., Robinson, J.B., Iacoviello, F., Finegan, D.P., Brett, D.J.L., Shearing, P.R., 2017. Three-phase segmentation of solid oxide fuel cell anode materials using lab based X-ray nano-computed tomography. Fuel Cells 17 (1), 75–82.

Heenan, T.M.M., Brett, D.J.L., Shearing, P.R., 2017. X-ray attenuation properties of commonly employed solid oxide fuel cell materials. Journal of Physics: Conference Series, June, vol. 849, no. 1. IOP Publishing, p. 012017.

Heenan, T.M.M., Robinson, J.B., Lu, X., Tjaden, B., Cervellino, A., Bailey, J.J., Brett, D.J. L., Shearing, P.R., 2018. Understanding the thermo-mechanical behaviour of solid oxide fuel cell anodes using synchrotron X-ray diffraction. Solid State Ionics 314, 156–164.

Heenan, T.M.M., Lu, X., Iacoviello, F., Robinson, J.B., Brett, D.J.L., Shearing, P.R., 2018. Thermally driven SOFC degradation in 4D: Part I. Microscale. J. Electrochem. Soc. 165 (11), F921–F931.

Heenan, T.M.M., Finegan, D.P., Tjaden, B., Lu, X., Iacoviello, F., Millichamp, J., Brett, D. J., Shearing, P.R., 2018. 4D nano-tomography of electrochemical energy devices using lab-based X-ray imaging. Nano Energy 47, 556–565.

Iwai, H., Shikazono, N., Matsui, T., Teshima, H., Kishimoto, M., Kishida, R., Hayashi, D., Matsuzaki, K., Kanno, D., Saito, M., Muroyama, H., 2010. Quantification of SOFC anode microstructure based on dual beam FIB-SEM technique. J. Power Sour. 195 (4), 955–961.

Izzo, J.R., Joshi, A.S., Grew, K.N., Chiu, W.K., Tkachuk, A., Wang, S.H., Yun, W., 2008. Nondestructive reconstruction and analysis of SOFC anodes using X-ray computed tomography at sub-50 nm resolution. J. Electrochem. Soc. 155 (5), B504–B508.

Kirchner, J.W., Feng, X., Neal, C., 2000. Fractal stream chemistry and its implications for contaminant transport in catchments. Nature 403 (6769), 524.

Laurencin, J., Quey, R., Delette, G., Suhonen, H., Cloetens, P., Bleuet, P., 2012. Characterisation of Solid Oxide Fuel Cell Ni–8YSZ substrate by synchrotron X-ray nano-tomography: from 3D reconstruction to microstructure quantification. J. Power Sour. 198, 182–189.

Lu, X., Heenan, T.M., Bailey, J.J., Li, T., Li, K., Brett, D.J., Shearing, P.R., 2017. Correlation between triple phase boundary and the microstructure of Solid Oxide Fuel Cell anodes: the role of composition, porosity and Ni densification. J. Power Sour. 365, 210–219.

Lu, X., Li, T., Bertei, A., Cho, J., Heenan, T., Rabuni, M., Li, K., Brett, D., Shearing, P., 2018. The Application of Hierarchical Structures in Energy Devices: New Insights into the Design of Solid Oxide Fuel Cells with Enhanced Mass Transport. Energy & Environmental Science.
Mandelbrot, B., 1967. How long is the coast of Britain? Statistical self-similarity and fractional dimension. Science 156 (3775), 636–638.
Mandelbrot, B.B., Passoja, D.E., Paullay, A.J., 1984. Fractal character of fracture surfaces of metals. Nature 308 (5961), 721.
Miller, K.J., Berendsen, S., Seute, T., Yeom, K., Gephardt, M.H., Grant, G.A., Robe, P.A., 2017. Fractal Structure in the Volumetric Contrast Enhancement of Malignant Gliomas as a Marker Of Oxidative Metabolic Pathway Gene Expression. Translational Cancer Research.
Ormerod, R.M., 2003. Solid oxide fuel cells. Chem. Soc. Rev. 32 (1), 17–28.
Park, K., Yu, S., Bae, J., Kim, H., Ko, Y., 2010. Fast performance degradation of SOFC caused by cathode delamination in long-term testing. Int. J. Hydrogen Energy 35 (16), 8670–8677.
Rueden, C.T., Schindelin, J., Hiner, M.C., DeZonia, B.E., Walter, A.E., Arena, E.T., Eliceiri, K.W., 2017. Image J2: ImageJ for the next generation of scientific image data. BMC Bioinf. 18 (1), 529.
Scrosati, B., 2000. Recent advances in lithium ion battery materials. Electrochim. Acta 45 (15–16), 2461–2466.
Serov, A., Kwak, C., 2009. Review of non-platinum anode catalysts for DMFC and PEMFC application. Appl. Catal. B 90 (3–4), 313–320.
Shah, S.M., Gray, F., Crawshaw, J.P., Boek, E.S., 2016. Micro-computed tomography pore-scale study of flow in porous media: Effect of voxel resolution. Adv. Water Resour. 95, 276–287.
Shearing, P.R., Golbert, J., Chater, R.J., Brandon, N.P., 2009. 3D reconstruction of SOFC anodes using a focused ion beam lift-out technique. Chem. Eng. Sci. 64 (17), 3928–3933.
Shearing, P.R., Cai, Q., Golbert, J.I., Yufit, V., Adjiman, C.S., Brandon, N.P., 2010. Microstructural analysis of a solid oxide fuel cell anode using focused ion beam techniques coupled with electrochemical simulation. J. Power Sour. 195 (15), 4804–4810.
Shearing, P.R., Gelb, J., Brandon, N.P., 2010. X-ray nano computerised tomography of SOFC electrodes using a focused ion beam sample-preparation technique. J. Eur. Ceram. Soc. 30 (8), 1809–1814.
Tikhomirov, G., Petersen, P., Qian, L., 2017. Fractal assembly of micrometre-scale DNA origami arrays with arbitrary patterns. Nature 552 (7683), 67.
Timurkutluk, B., Mat, M.D., 2016. A review on micro-level modeling of solid oxide fuel cells. Int. J. Hydrogen Energy 41 (23), 9968–9981.
Tjaden, B., Brett, D.J., Shearing, P.R., 2018. Tortuosity in electrochemical devices: a review of calculation approaches. Int. Mater. Rev. 63 (2), 47–67.
Wilson, J.R., Kobsiriphat, W., Mendoza, R., Chen, H.Y., Hiller, J.M., Miller, D.J., Thornton, K., Voorhees, P.W., Adler, S.B., Barnett, S.A., 2006. Three-dimensional reconstruction of a solid-oxide fuel-cell anode. Nat. Mater. 5 (7), 541.
Yousuf, M., Sahu, P.C., Rajan, K.G., 1986. High-pressure and high-temperature electrical resistivity of ferromagnetic transition metals: nickel and iron. Phys. Rev. B 34 (11), 8086.
Zekri, A., Herbrig, K., Knipper, M., Parisi, J., Plaggenborg, T., 2017. Nickel depletion and agglomeration in SOFC anodes during long-term operation. Fuel Cells 17 (3), 359–366.
Zhou, H.W., Zhong, J.C., Ren, W.G., Wang, X.Y., Yi, H.Y., 2018. Characterization of pore-fracture networks and their evolution at various measurement scales in coal samples using X-ray μCT and a Fractal method. Int. J. Coal Geol. 189, 35–49.
Zhu, W.Z., Deevi, S.C., 2003. A review on the status of anode materials for solid oxide fuel cells. Mater. Sci. Eng., A 362 (1–2), 228–239.
Zhu, H., Kee, R.J., 2003. A general mathematical model for analyzing the performance of fuel-cell membrane-electrode assemblies. J. Power Sour. 117 (1–2), 61–74.